Nano Research

Open Access

Research Article

Boosting methanol electro-oxidation to formate by trace iron induced suppression of cobalt(IV) formation

Jialong Lin[1], Xinlin Wang[1], Bingxue Cheng[1], Ruiheng Zhou[1], Yuhang Li[2], Tamao Ishida[3], Guangli Xiu[1], Toru Murayama[4] ✉, and Mingyue Lin[1,5] ✉

[1] *State Environmental Protection Key Laboratory of Environmental Risk Assessment and Control on Chemical Process, Shanghai Environmental Protection Key Laboratory on Environmental Standard and Risk Management of Chemical Pollutants, School of Resources and Environmental Engineering, East China University of Science and Technology, Shanghai 200237, China*
[2] *School of Materials Science and Engineering, East China University of Science and Technology, Shanghai 200237, China*
[3] *Department of Applied Chemistry for Environment, Graduate School of Urban Environmental Sciences, Tokyo Metropolitan University, Tokyo 192-0397, Japan*
[4] *Institute for Catalysis, Hokkaido University, Hokkaido 001-0021, Japan*
[5] *Shanghai Institute of Pollution Control and Ecological Security, Shanghai 200092, China*

Cite this article: *Nano Research*, **2025**, *18*, 94907389. https://doi.org/10.26599/NR.2025.94907389

ABSTRACT: Converting methanol to high-value formate through electrochemical methods can significantly reduce the energy consumption associated with conventional production processes. In this study, we directly synthesized iron-doped cobalt phosphate (Fe-CoPO) on nickel foam (NF) to achieve excellent activity for the methanol electro-oxidation reaction (MOR). Our results demonstrated that Fe-CoPO produced a current density of 100 mA·cm^{-2} at a significantly low operating potential of 1.436 V (vs. reversible hydrogen electrode (RHE)) and operated steadily for 16 h at this current density with a Faradaic efficiency (FE) of 97%. Furthermore, Fe-CoPO maintained a high FE of 100% even at an extremely high current density of 300 mA·cm^{-2} for 8 h. We found that the high MOR activity of Fe-CoPO results from electrochemical reconstruction to generate the $Co^{2+/3+}$–O bond. The heterogeneous interface between Fe and Co inhibits the formation of Co^{4+}, which significantly enhances the MOR activity. Thus, this work not only provides insights into the mechanism of MOR over Co-based catalysts but also offers a novel direction for developing highly active MOR catalysts.

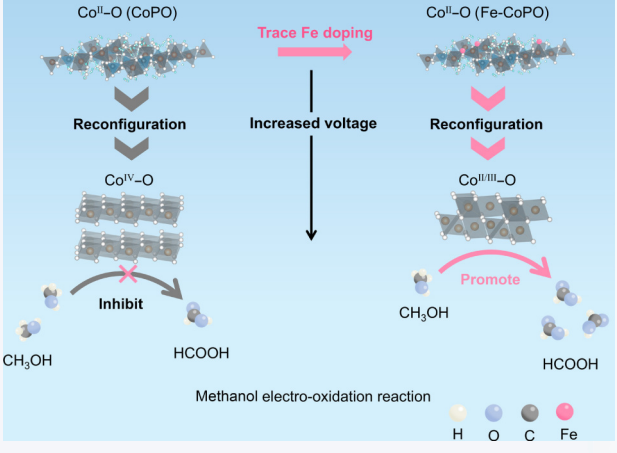

KEYWORDS: cobalt phosphate, methanol electro-oxidation reaction, formate, Fe doping, electrocatalysis

1 Introduction

Hydrogen production via electrocatalytic reduction of abundant water resources has received much attention in recent years as a response to climate and environmental change and to address energy shortages. However, the anodic oxygen precipitation reaction paired with this cathodic half-reaction in this process involves multiple intermediate valence change steps, leading to complex catalytic cycle kinetics and overall slow catalytic kinetics [1, 2]. In recent years, the oxygen evolution reaction (OER) has been replaced by the methanol electro-oxidation reaction (MOR) because MOR is thermodynamically more favorable for coupling with cathodic half-reactions, thereby improving electrical energy utilization [3–5]. Currently, in conventional industrial production, formic acid is synthesized through the carbonylation of methanol using toxic and explosive carbon monoxide to produce methyl formate, which is subsequently hydrolyzed to formic acid under high temperature (413 K) and high pressure (4 MPa). In contrast, obtaining formic acid by MOR overcomes the disadvantages of high temperature and high pressure required for the industrial production of formic acid [6–8]. Most precious metal catalysts in current MORs typically convert methanol to carbon dioxide instead

Received: December 31, 2024; **Revised:** March 14, 2025
Accepted: March 17, 2025

✉Address correspondence to Toru Murayama, murayama@cat.hokudai.ac.jp; Mingyue Lin, ms.mingyuelin@ecust.edu.cn

of formic acid [9]. Designing non-precious metal electrocatalysts with high formate selectivity and elucidating their mechanisms in the MOR is essential for advancing methanol electro-oxidation technology.

It is widely recognized that transition metal-based materials primarily act as pre-catalysts in electrocatalytic processes. Under alkaline conditions, these materials can undergo substantial structural reconstruction, leading to the generation of new coordination environments and enhanced catalytic activity [10, 11]. Previous studies have demonstrated that P-substituted $CoSe_2$ undergoes structural transformation in alkaline media, resulting in the formation of truly active sites [11]. Consequently, the development of pre-catalysts capable of facilitating such reconstructions to produce active sites represents an ideal strategy for catalyst design. For instance, iron and cobalt phosphates (CoPO) have emerged as a prominent research focus in this field. Both iron and cobalt exhibit excellent redox properties and high electrical conductivity [12–15]. When combined into a composite material, the Fermi energy level difference between the iron and cobalt components modulates the electron distribution, thereby enhancing the electron transfer rate, accelerating the formation of active species, and improving the catalytic activity for the MOR [16–20]. When used as pre-catalysts for MOR, iron and CoPO facilitate catalyst reconstruction and the generation of active sites [20–22]. For example, studies have shown that Co_2P undergoes a complete phase transition to cobalt hydroxide in alkaline electrolytes, significantly boosting the reaction rate [23].

We synthesized iron-doped CoPO (Fe-CoPO) on a nickel foam (NF) substrate. Fe-CoPO provides a large current density of 100 mA·cm^{-2} at a remarkably low working potential of 1.436 V. Furthermore, even under the extremely high current density of 300 mA·cm^{-2} for 8 h, the FE remains 100%. Surprisingly, *in situ* Raman spectrum investigations show subtle differences in the Co chemical state between the CoPO and Fe-CoPO. As depicted in Scheme 1, we observed that the Co^{2+}–O bond in CoPO undergoes electrochemical reconstruction, transforming into the Co^{4+}–O bond. Co^{4+} species, widely recognized as catalytically active sites for OER, competitively occupy surface reactive centers essential for methanol adsorption and C–H bond activation. This site-competitive mechanism results in the kinetic suppression of MOR activity. Therefore, we proposed that Fe doping inhibited the oxidation of Co^{3+} to Co^{4+} and promoted the generation of the $Co^{2+/3+}$–O bond, thus enhancing the MOR activity.

2 Experimental section

2.1 Preparation of catalysts

The Fe-CoPO catalyst was synthesized using a one-pot hydrothermal method. First, the NF was sonicated in a 1:1 solution of acetone and hydrochloric acid (1 mol·L^{-1}) for 5 min, followed by sonication in deionized water for another 5 min. Next, $Na_2HPO_4{\cdot}12H_2O$ (1.07 g) and hexadecyl trimethyl ammonium bromide (CTAB, 0.364 g) were dissolved in a solution (water (12 mL) and ethylene glycol (8 mL)) with continuous stirring. Subsequently, $Co(NO_3)_2{\cdot}6H_2O$ (0.873 g) and $Fe(NO_3)_3{\cdot}9H_2O$ (0.202, 0.606, and 1.212 g) were added to this solution, and the mixture was stirred for 20 min to obtain a light pink precursor solution. Then, the mixture solution with pre-cleaned NF was refrigerated overnight. The mixture was then subjected to hydrothermal treatment at 160 °C for 10 h. After cooling to room temperature, the sample was rinsed with deionized water and then dried overnight in an oven. The amount of doping Fe in the prepared CoPO was determined to be 1.19 wt.%, 2.44 wt.%, and 5.57 wt.% according to inductively coupled plasma mass spectrometry (ICP-MS) analysis, respectively, and were named as Fe-CoPO-L, Fe-CoPO, Fe-CoPO-H, respectively.

CoPO was fabricated using a comparable process applied for the synthesis of Fe-CoPO, except no Fe source was added.

2.2 Materials characterization

Scanning electron microscopy (SEM, Apreo 2 C) measurement was utilized to analyze the structures of the catalysts. Energy-dispersive X-ray spectroscopy (EDS) mapping images were gained on the ZEISS GeminiSEM 300 instrument. X-ray diffraction (XRD, Rigaku SmartLab SE) measurement was employed to determine the phase composition of the catalysts, utilizing a Cu Kα radiation source (λ = 1.54 Å). X-ray photoelectron spectroscopy (XPS, ESCALAB 250Xi) measurement with an Al Kα excitation source was used to examine

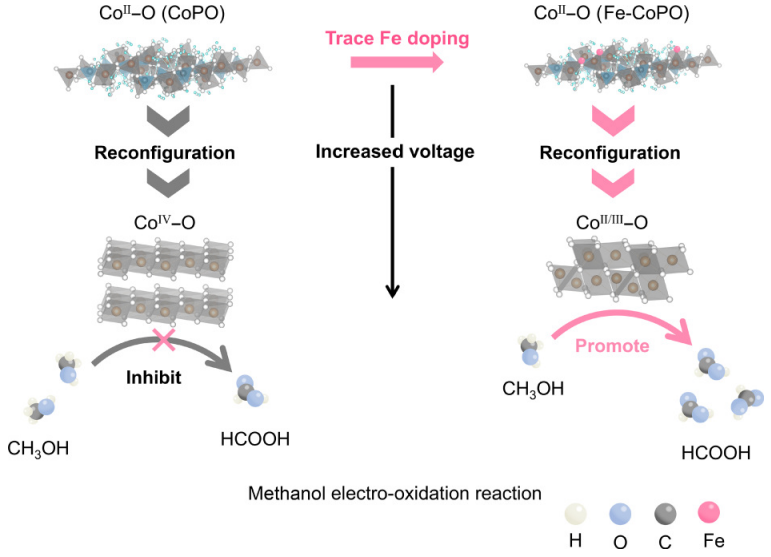

Scheme 1 With the increased applied voltage, the Co^{II}–O bond in CoPO is converted to the Co^{IV}–O bond, while the Co^{II}–O bond in Fe-CoPO is converted to the Co$^{II/III}$–O bond.

the chemical states of the elements in the catalyst. The *operando* Raman measurements (Renishaw inVia Reflex Raman system) were conducted using an excitation source of laser wavelength of 532 nm. The *in situ* experiments were carried out using customized electrochemical cell (Fig. S1 in the Electronic Supplementary Material (ESM)). To analyze the products in the electrolyte, 500 μL of the electrolyte solution was mixed with 100 μL of D_2O (containing 0.05 wt.% tris(trimethylsilyl)phosphate (TMSP) as an internal standard) and transferred into a nuclear magnetic resonance (NMR) tube. The mixture was thoroughly homogenized prior to analysis. Subsequently, the samples were analyzed using NMR spectroscopy to determine the overall intensity of the formate ion signal. The yield of formate generated in the electrolyte was quantified by calculating the integral ratio of the proton peaks of formate and the internal standard. The NMR tests were conducted with an Ascend 600 instrument (Bruker).

3 Results and discussion

3.1 Synthesis and characterization of Fe-CoPO

NF serves as a supportive substrate characterized by high electrical conductivity and a three-dimensional (3D) microporous structure, which facilitates the uniform distribution of catalysts [24]. We deposited Fe-CoPO nanoflower arrays on NF using a one-pot hydrothermal method (Fig. S2 in the ESM) [25].

The surface morphology of Fe-CoPO was evaluated through SEM measurement. The SEM images (Figs. 1(a)–1(c)) of Fe-CoPO reveal that the NF skeleton is enveloped by a uniformly distributed catalytic material. This uniformly distributed catalytic layer exposes a greater number of active sites [26–28]. Interestingly, the SEM images (Figs. S3(a)–S3(d) in the ESM) of undoped versus Fe-doped CoPO display intricate nanosheet structures, suggesting that Fe doping contributes to the reorganization of CoPO on the NF surface, resulting in relatively stable surface composition and structure. The SEM images of elements (Figs. 1(d)–1(g)) show the presence of the elements P, Fe, Co, and Ni. The EDS mapping image is shown in Fig. S4 in the ESM.

We employed Raman spectroscopy to analyze the physical phase composition of the Fe-CoPO (Fig. S5 in the ESM), which revealed characteristic peaks corresponding to Co–O bonds and PO_4^{3-} groups. Due to the influence of the NF substrate, it was difficult to distinguish the main phase of the material in the XRD pattern of the whole electrode (Fig. S6 in the ESM). Therefore, we collected

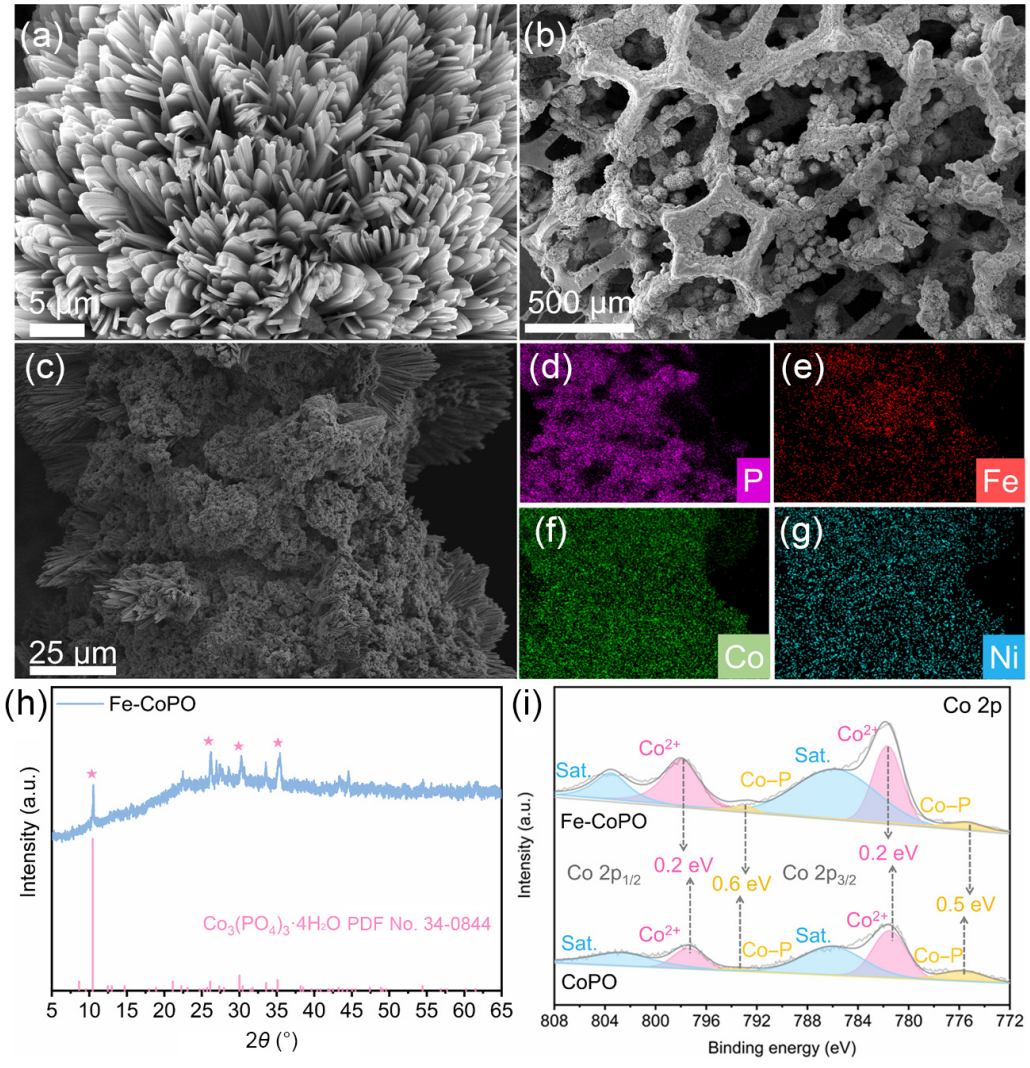

Figure 1 ((a)–(c)) SEM images of the Fe-CoPO. ((d)–(g)) Elemental mappings of P, Fe, Co, and Ni in Fe-CoPO. (h) XRD pattern of Fe-CoPO. (i) XPS spectra of Co 2p of Fe-CoPO and CoPO.

powders on NF substrates to conduct the XRD measurement. In the XRD pattern of Fe-CoPO (Fig. 1(h)), we observed the diffraction peak at 10.4° corresponds to the (020) crystal plane of $Co_3(PO_4)_2{\cdot}4H_2O$ (JCPDS No. 34-0844) exhibiting an orthorhombic crystal structure.

We analyzed the valence electron interactions of Fe-CoPO and CoPO surface materials using XPS measurement. As shown in Fig. 1(i), the Co 2p XPS spectrum of Fe-CoPO had peaks at 781.7 and 798.0 eV, which can be attributed to Co^{2+}, which is consistent with the position of typical Co^{2+} peaks in $Co_3(PO_4)_2{\cdot}4H_2O$ [29]. A weak and broad peak at 775.3 and 792.8 eV, which is located in the same position as the reported cobalt–phosphorus–oxygen bond (Co–P–O), suggests the possible existence of interfacial interactions [30, 31]. The peaks corresponding to Co^{2+} bonds in Fe-CoPO show a positive shift in binding energy as compared to CoPO, indicating the presence of significant electronic interactions between Fe and CoPO. On the other hand, the Co–P bond in Fe-CoPO exhibits a negative shift compared to CoPO, indicating that the electron density of the Co site in Fe-CoPO has increased. The XPS spectrum of Fe 2p (Fig. S7(a) in the ESM). The peaks at 711.3 eV (Fe^{2+} $2p_{3/2}$) and 713.3 eV (Fe^{3+} $2p_{3/2}$) were observed. This observation indicates the coexistence of Fe^{2+} and Fe^{3+} in Fe-CoPO [32]. In the XPS spectrum of O 1s (Fig. S7(b) in the ESM), distinct peaks at 531.1 and 532.8 eV correspond to the reverse convolution of PO_4^{3-} and adsorbed H_2O, respectively [33]. XPS result reveals that the Co^{2+} peak shifts to higher binding energy, while the Co–P peak redshifts. This observation highlights the synergistic interaction between Fe and Co, wherein electronic interactions and charge redistribution promote efficient electron transfer from Fe to Co.

3.2 MOR performance of Fe-CoPO in alkaline medium

The MOR performance of the as-synthesized samples was investigated using linear sweep voltammetry (LSV) measurement. It was observed that the Fe:Co ratio in Fe-CoPO significantly influences its catalytic activity. Notably, Fe-CoPO (Fe = 2.44 wt.%) exhibited the highest MOR performance (Fig. S8 in the ESM). As shown in Fig. S9 in the ESM, the addition of methanol to the alkaline electrolyte significantly reduces the potential required to achieve a specific current density. This reduction is likely due to the much lower thermodynamic equilibrium potential for methanol electro-oxidation compared to that of OER. The LSV curves (Fig. 2(a)) of Fe-CoPO show a clear oxidation peak, which is due to the formation of Co^{3+} [5, 34–37]. The LSV curves (Fig. 2(a)) (without *iR* compensation) show that Fe-CoPO electrochemically outperforms CoPO. For the CoPO catalyst, the potential required to achieve a current density of 10 mA·cm^{-2} is 1.382 V (Fig. 2(b)). Trace Fe doping in CoPO significantly reduces the CoPO potential from 1.382 to 1.284 V (Fe-CoPO), a decrease of 98 mV. At 100 mA·cm^{-2} current density, the potential of Fe-CoPO was the lowest at 1.436 V, much lower than that of CoPO (1.504 V) and NF (1.597 V). A trace amount of Fe doping (2.44 wt.%) significantly

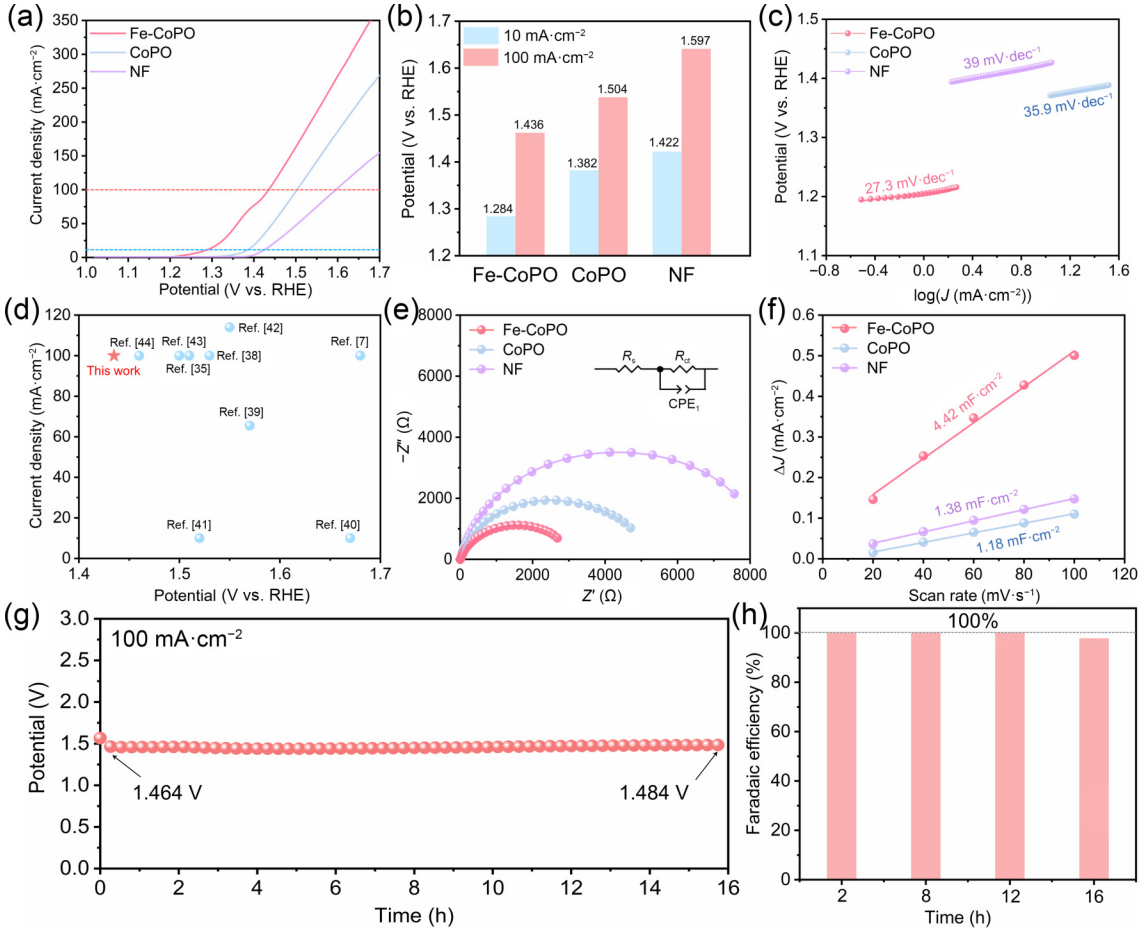

Figure 2 (a) LSV MOR curves, (b) potential, and (c) Tafel slope of Fe-CoPO, CoPO, and NF in 1 M KOH with 1 M methanol. (d) Comparison of electrocatalytic performance of different electrocatalysts [7, 35, 38–44]. (e) Nyquist plots and (f) C_{dl} of Fe-CoPO, CoPO, and NF. (g) Stability test of Fe-CoPO at 100 mA·cm^{-2}. (h) FE of formate obtained at different times on Fe-CoPO.

enhances the electrochemical activity, as evidenced by the reduction of the overpotential from 1.504 to 1.436 V. This observation further corroborates the synergistic interaction between Fe and Co, which effectively facilitates charge transfer kinetics. The Tafel slope (Fig. 2(c)) of Fe-CoPO was 27.3 mV·dec^{-1}, significantly lower than that of CoPO (35.9 mV·dec^{-1}) and NF (39 mV·dec^{-1}). This indicates that the synergistic interaction between Fe and Co enhances the MOR kinetics and electrocatalytic activity, surpassing the performance of the best catalyst reported previously (Fig. 2(d)). Electrochemical impedance spectroscopy (EIS) measurement further analyzes the charge transfer ability. The EIS plots (Fig. 2(e)) show a lower value of charge-transfer resistance (R_{ct}, 2.8 Ω) for Fe-CoPO as compared to CoPO (3.26 Ω), revealing favorable charge transfer kinetics of the Fe-CoPO electrode. Furthermore, to assess the catalytic efficiency of the Fe-CoPO electrodes, the electrochemical double layer capacitance (C_{dl}) in the non-Faradic region, which is typically used to quantify electrochemical active surface area (ECSA), was measured (Figs. S10(a)–S10(c) in the ESM). Fe-CoPO (Fig. 2(f)) has the largest C_{dl} of 4.42 mF·cm^{-2} compared to other samples, indicating that more reactive sites are exposed in Fe-CoPO.

Based on these experimental results, the enhancement in MOR activity is primarily attributed to the synergistic interaction between Fe and Co, as well as the increased ECSA induced by Fe doping, which leads to the formation of additional active sites.

Chronopotentiometry (CP) was used to perform the selective MOR testing on Fe-CoPO. As demonstrated in Fig. 2(g), Fe-CoPO was operated for at least 16 h at a current density of 100 mA·cm^{-2}, and the oxidation potential of the electrode increased by only 20 mV, indicating excellent long-term stability. The electrolyte was collected at regular intervals, and the formate FE was measured by ^{1}H-NMR analysis. During methanol electro-oxidation, the FE of formate was about 100% (Fig. 2(h)). As demonstrated in Fig. S11 in the ESM, the formate level gradually increased during the reaction but did not decrease. Fe-CoPO remained stable at high current densities of 200 and even 300 mA·cm^{-2} (Fig. S12(a) in the ESM). Notably, the FE of Fe-CoPO formate remained at 100% even at a high current density of 300 mA·cm^{-2} (Fig. S12(b) in the ESM).

To explore the durability of the morphological structure, we measured the SEM images of Fe-CoPO after 8 h. SEM images (Figs. S13(a) and S13(b) in the ESM) revealed that the catalyst surface still contained a substantial number of nanoflower structures. The excellent stability of Fe-CoPO is likely attributed to the *in situ* growth of the catalytically active phase on a conductive NF substrate. This configuration facilitates rapid charge transfer without the need for additional binders, and the strong adhesion helps prevent catalyst slippage. Confirmation of the high efficiency and outstanding stability of Fe-CoPO in the production of formate through methanol electro-oxidation.

3.3 Insights into the mechanism of MOR

XPS measurement was used to analyze changes in the valence states of elements on the catalyst surface before and after 8 h of the MOR reaction. The spectrum of Fe 2p of Fe-CoPO before and after the reaction is shown in Fig. S14 in the ESM. The comparative analysis of the Ni 2p spectra (Fig. S15 in the ESM) for Fe-CoPO catalysts in both pre- and post-reaction states showed no significant changes in the oxidation states of the Ni species. This observation suggests that Ni species did not participate in the MOR. The Co 2p XPS spectra (Fig. 3(a)) of Fe-CoPO are moved to smaller values compared to the sample before MOR, suggesting that Co lost electrons during the reaction process. Simultaneously, the Co^{3+} content increases in the post-test Fe-CoPO. Besides, the spectrum of O 1s of Fe-CoPO after the reaction (Fig. 3(b)) shows that, in addition to the peaks of hydroxide and adsorbed water, a new peak attributed to metal-oxygen bonding (Co–O) appeared at 529.3 eV, confirming the formation of the $Co^{2+/3+}$–O bond following the MOR reaction. This indicates that $Co^{2+/3+}$–O could be the active site of Fe-CoPO for MOR. In contrast, the Co 2p and O 1s spectra of CoPO (Figs. S16(a) and S16(b) in the ESM) revealed a distinct Co^{4+} peak at 782.3 eV and Co^{4+}–O peak at 529.4 eV after MOR, suggesting a different oxidation pathway between Fe-CoPO and CoPO [45–48].

To further elucidate the role of Co valence states in MOR activity, *in situ* Raman spectroscopy was performed for Fe-CoPO and CoPO to gain an in-depth understanding of how Fe doping promotes MOR. Under open circuit potential (OCP) conditions (Fig. 3(c)), the Raman scattering modes of the CoPO samples at 437.5, 504.4, and 684.8 cm^{-1} are attributed to the E_g vibrational modes of Co^{4+}–O, CoOOH, and the A_{1g} symmetric stretching mode of $Co^{2+/3+}$–O [49–54]. In *operando* Raman spectroscopic studies, the energy band of CoPO at 437 cm^{-1} gradually increases with the applied potential, indicating an increase in Co^{4+}–O content in the catalyst and a deeper reconstruction [55]. The above results indicate that CoPO undergoes three reconstruction steps under alkaline conditions: Co^{2+}–O → Co^{3+}–O → Co^{4+}–O, which is consistent with the thermodynamic theory of the transition due to the increase in potential [56]. On the contrary, the Co^{4+}–O bond could not be detected in the Raman spectra of Fe-CoPO (Fig. 3(d)). The characteristic peaks in the Raman spectra of Fe-CoPO are somewhat red-shifted concerning CoPO because the radius of Fe ions is larger than that of Co ions. The characteristic peak of the $Co^{2+/3+}$–O bond (A_{1g}) steadily increases as the applied voltage increases from 1.03 to 1.63 V. CoPO and Fe-CoPO were subjected to CP tests (Fig. 3(e)) for 12 h. The CP results (Fig. 3(f)) showed that Fe-CoPO had 100% formate selectivity, whereas the formate Faradaic efficiency (FE) of CoPO was only 39.7%. In addition, only the characteristic peaks of formate and methanol were observed in the ^{13}C-NMR analysis of CoPO (Fig. S17 in the ESM), further confirming the limited conversion of methanol to formate on Co^{4+}. In the MOR process, Co^{4+}–O formed by electrochemical reconstruction of CoPO during the MOR process has been considered to have excellent OER catalytic activity [57, 58]. Under alkaline conditions, adjacent OH^- attacks the oxygen ligands in Co^{4+}–O to form intramolecular O–O bond, facilitating rapid OER kinetics [59]. Thus, OER and MOR competition occurred at the Co^{4+}–O, inhibiting MOR. Whereas $Co^{2+/3+}$–O formed by electrochemical reconstruction of Fe-CoPO facilitated the formation of formate. The above experimental results demonstrated that $Co^{2+/3+}$–O is the catalytically active site for formate in the MOR process.

In addition, to demonstrate the existence of interaction between Fe and Co components in Fe-CoPO, *in situ* Raman measurements were performed on Fe-CoPO-L and Fe-CoPO-H. As shown in Fig. S18(a) in the ESM, the Co^{4+}–O bond was also observed for Fe-CoPO-L, which is similar to CoPO. The Raman spectra of Fe-CoPO-H (Fig. S18(b) in the ESM) show no Co^{4+}–O bond generation, and the characteristic Raman scattering peak at 685.3 cm^{-1} can be attributed to $Co^{2+/3+}$–O. However, when the applied potential was increased from 1.03 to 1.63 V (vs. reversible hydrogen electrode (RHE)), the strength of the $Co^{2+/3+}$–O peak gradually decreased with the increase in the applied voltage.

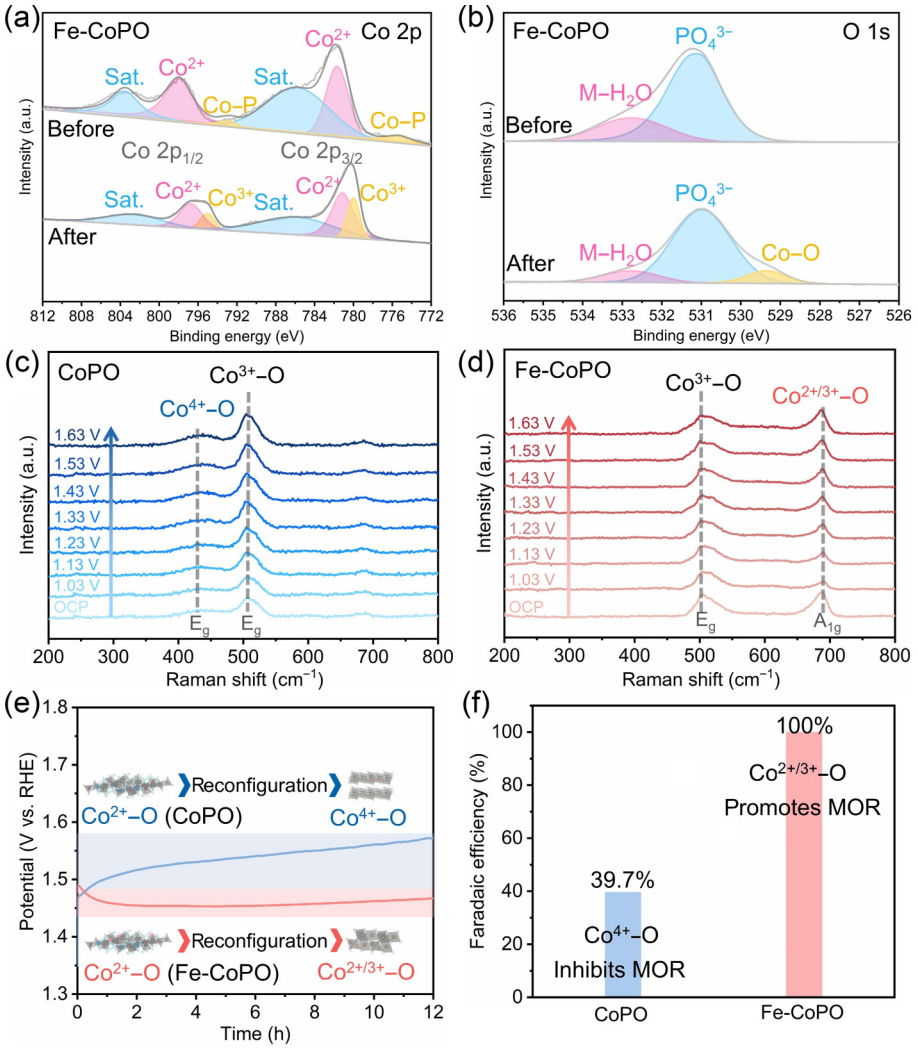

Figure 3 XPS spectra of (a) Co 2p and (b) O 1s for Fe-CoPO after MOR. *In situ* Raman spectra measurements of (c) CoPO and (d) Fe-CoPO. (e) CP curves of CoPO and Fe-CoPO at 100 mA·cm^{-2}. (f) FE of formate on CoPO and Fe-CoPO.

Therefore, in combination with the above Raman spectroscopic investigation, Fe doping can inhibit the oxidation of $Co^{2+/3+}$ to Co^{4+}, thereby inhibiting the competition for OER during the MOR process. Promote the electrochemical reconstruction of the Co^{2+}–O bond in Fe-CoPO to form the $Co^{2+/3+}$–O bond, thereby enhancing MOR activity.

Based on the above experimental results, we propose the existence of a Co^{2+}/Co^{3+} cycling pathway for the MOR in Fe-CoPO. Trace Fe doping modifies the crystal structure of Fe-CoPO, facilitating its electrochemical reconstruction and the formation of the $Co^{2+/3+}$–O bond, thereby enhancing formate selectivity [60, 61]. The reaction pathway for MOR on Fe-CoPO is illustrated in Fig. 4. First, Fe-CoPO undergoes electrochemical reconfiguration at a certain potential, inducing the formation of the Co^{2+}/Co^{3+}–O bond through moderate Fe doping. Co^{2+} is oxidized to Co^{3+} at certain potentials, which is consistent with the Co^{2+} to Co^{3+} oxidation peaks observed in the LSV curves [62]. Methanol spontaneously adsorbs on the Co^{3+} sites (Eq. (1)) [63, 64]. Under alkaline conditions, OH^- in water directly attacks the nucleophilic methanol, thereby oxidizing it via a direct oxidation pathway [65, 66]. Specifically, OH^- deprotonates the hydrogen atom of CH_3OH to produce the intermediate *CHO (Eqs. (2)–(4)), which then reacts with OH^- in a nucleophilic oxidation reaction to yield $HCOO^-$ (Eq. (5))

$$Co(III) + CH_3OH \rightarrow Co(III) - CH_3OH \quad (1)$$

$$Co(III) - CH_3OH + OH^- \rightarrow Co(III) - {}^*CH_3O + H_2O + e^- \quad (2)$$

$$Co(III) - {}^*CH_3O + OH^- \rightarrow Co(III) - {}^*CH_2O + H_2O + e^- \quad (3)$$

$$Co(III) - {}^*CH_2O + OH^- \rightarrow Co(III) - {}^*CHO + H_2O + e^- \quad (4)$$

$$Co(III) - {}^*CHO + OH^- \rightarrow Co(III) - HCOO^- \quad (5)$$

During the oxidation of methanol to formate, Co^{3+} is simultaneously reduced back to Co^{2+}, establishing a stable Co^{2+}/Co^{3+} redox cycle. This cycling mechanism enables the Fe-CoPO catalyst to sustain its electrocatalytic activity in the MOR, allowing Co ions to continuously transition between Co^{2+} and Co^{3+} while facilitating electron transfer to methanol along the reaction pathway.

4 Conclusion

In summary, we have demonstrated that the Fe-CoPO catalyst exhibits significantly enhanced performance through the

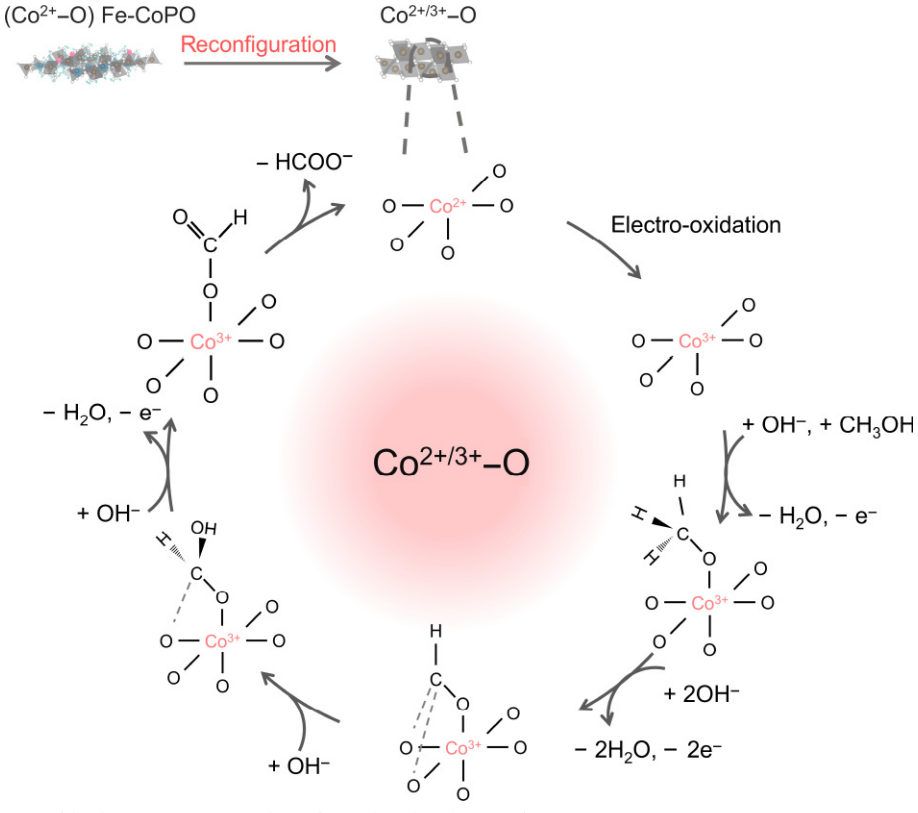

Figure 4 Schematic illustration of the dominant reaction pathway for methanol oxidation to formate over Fe-CoPO.

introduction of Fe ions into CoPO, resulting in exceptional electrocatalytic activity. The catalyst operated at a minimum potential of 1.436 V at 100 mA·cm^{-2} and maintained 97% formate selectivity for 16 h of stable operation at this current density. Even more encouragingly, the FE of formate remained at 100% for 8 h at higher current densities (200–300 mA·cm^{-2}). Furthermore, the production and dynamics of active substances on the catalyst surface were tracked using *in situ* Raman measurements to gain insight into the Fe-CoPO surface reconstruction during the MOR process. We proposed that the introduction of Fe promoted the electrochemical reconstruction of the Co^{2+}–O bond in Fe-CoPO, leading to the formation of the $Co^{2+/3+}$–O bond. In contrast, the Co^{2+}–O bond in CoPO was transformed into the Co^{4+}–O bond. The synergistic interaction between Fe and Co might inhibit Co peroxidation and minimize Co^{4+} generation, allowing for a reversible redox shift of $Co^{2+/3+}$.

In conclusion, our findings provide valuable insights into the logical and precise design of effective MOR electrocatalysts based on transition metal phosphides. Looking ahead, further investigations into the mechanism of iron–cobalt interactions, as well as the exploration of alternative transition metal doping strategies, could facilitate the development of more efficient catalysts. Additionally, the long-term stability of the Fe-CoPO catalyst under practical conditions warrants further study.

Electronic Supplementary Material: Supplementary material (detailed description of experimental procedures, spectroscopic data (Raman spectra, EDS mapping image, and XPS spectra), materials characterization data (SEM images), and electrocatalytic performances data) is available in the online version of this article at https://doi.org/10.26599/NR.2025.94907389.

Data availability

All data needed to support the conclusions in the paper are presented in the manuscript and the Electronic Supplementary Material. Additional data related to this paper may be requested from the corresponding author upon request.

Acknowledgements

We acknowledge the financial support from the National Key Research and Development Program of China (No. 2022YFC3703503), the Science and Technology Commission of Shanghai Municipality (No. 24ZR1416000), and the Japan Society for the Promotion of Science (JSPS) through Grant-in-Aid for Scientific Research (Nos. 22H00282 and 23K26456). Additionally, this work was supported in part by Joint Usage/Research Center for Catalysis.

Declaration of competing interest

All the contributing authors report no conflict of interests in this work.

Author contribution statement

J. L. L: Writing – original draft, writing – review & editing, investigation, data curation. X. L. W.: Formal analysis. B. X. C.: Investigation. R. H. Z.: Investigation. Y. H. L.: Data curation, methodology. T. I.: Data curation, methodology. T. M.: Funding acquisition, supervision. G. L. X.: Project administration. M. Y. L.: Writing – review & editing, supervision, funding acquisition. All the authors have approved the final manuscript.

Use of AI statement

None.

References

[1] Ren, X.; Wu, T. Z.; Sun, Y. M.; Li, Y.; Xian, G. Y.; Liu, X. H.; Shen, C. M.; Gracia, J.; Gao, H. J.; Yang, H. T. et al. Spin-polarized oxygen evolution reaction under magnetic field. *Nat. Commun.* **2021**, *12*, 2608.

[2] Wen, Y. Z.; Liu, C.; Huang, R.; Zhang, H.; Li, X. B.; de Arquer, F. P. G.; Liu, Z.; Li, Y. Y.; Zhang, B. Introducing Brønsted acid sites to accelerate the bridging-oxygen-assisted deprotonation in acidic water oxidation. *Nat. Commun.* **2022**, *13*, 4871.

[3] Jiang, H.; Sun, M. Z.; Wu, S. L.; Huang, B. L.; Lee, C. S.; Zhang, W. J. Oxygen-incorporated NiMoP nanotube arrays as efficient bifunctional electrocatalysts for urea-assisted energy-saving hydrogen production in alkaline electrolyte. *Adv. Funct. Mater.* **2021**, *31*, 2104951.

[4] Guo, Y.; Yang, X. B.; Liu, X. C.; Tong, X. L.; Yang, N. J. Coupling methanol oxidation with hydrogen evolution on bifunctional Co-doped rh electrocatalyst for efficient hydrogen generation. *Adv. Funct. Mater.* **2023**, *33*, 2209134.

[5] Qi, Y. B.; Zhang, Y.; Yang, L.; Zhao, Y. H.; Zhu, Y. H.; Jiang, H. L.; Li, C. Z. Insights into the activity of nickel boride/nickel heterostructures for efficient methanol electrooxidation. *Nat. Commun.* **2022**, *13*, 4602.

[6] Duan, Z. Y.; Ren, T. L.; Mao, Q. Q.; Yu, H. J.; Deng, K.; Xu, Y.; Wang, Z. Q.; Wang, L.; Wang, H. L. Metal–organic framework derived Os-doped Ni_xP/N-doped carbon composite nanosheet arrays toward boosting methanol oxidation into value-added chemicals coupled with hydrogen production. *J. Mater. Chem. A* **2022**, *10*, 18126–18131.

[7] Hao, J.; Liu, J. W.; Wu, D.; Chen, M. X.; Liang, Y.; Wang, Q.; Wang, L.; Fu, X. Z.; Luo, J. L. *In situ* facile fabrication of $Ni(OH)_2$ nanosheet arrays for electrocatalytic co-production of formate and hydrogen from methanol in alkaline solution. *Appl. Catal. B: Environ.* **2021**, *281*, 119510.

[8] Yang, Q. F.; Zhang, C. J.; Dong, B.; Cui, Y. C.; Wang, F.; Cai, J. H.; Jin, P.; Feng, L. Synergistic modulation of nanostructure and active sites: Ternary Ru&Fe–WO_x electrocatalyst for boosting concurrent generations of hydrogen and formate over 500 $mA \cdot cm^{-2}$. *Appl. Catal. B: Environ.* **2021**, *296*, 120359.

[9] Bin, L.; Xiao, T. Y.; Sun, X. L.; Peng, H. Q.; Wang, X.; Zhao, Y. F.; Zhang, W. J.; Song, Y. F. Hierarchical trace copper incorporation activated cobalt layered double hydroxide as a highly selective methanol conversion electrocatalyst to realize energy-matched photovoltaic-electrocatalytic formate and hydrogen co-production. *J. Mater. Chem. A* **2022**, *10*, 19649–19661.

[10] Zheng, Y. R.; Wu, P.; Gao, M. R.; Zhang, X. L.; Gao, F. Y.; Ju, H. X.; Wu, R.; Gao, Q.; You, R.; Huang, W. X. et al. Doping-induced structural phase transition in cobalt diselenide enables enhanced hydrogen evolution catalysis. *Nat. Commun.* **2018**, *9*, 2533.

[11] Zhu, Y. P.; Chen, H. C.; Hsu, C. S.; Lin, T. S.; Chang, C. J.; Chang, S. C.; Tsai, L. D.; Chen, H. M. *Operando* unraveling of the structural and chemical stability of P-substituted $CoSe_2$ electrocatalysts toward hydrogen and oxygen evolution reactions in alkaline electrolyte. *ACS Energy Lett.* **2019**, *4*, 987–994.

[12] Zhang, K. X.; Zou, R. Q. Advanced transition metal-based OER electrocatalysts: Current status, opportunities, and challenges. *Small* **2021**, *17*, 2100129.

[13] Wang, P.; Qi, J.; Li, C.; Chen, X.; Wang, T. H.; Liang, C. H. N-doped carbon nanotubes encapsulating Ni/MoN heterostructures grown on carbon cloth for overall water splitting. *Chemelectrochem* **2020**, *7*, 745–752.

[14] Wu, B. Q.; Yang, Z. H.; Dai, X. P.; Yin, X. L.; Gan, Y. H.; Nie, F.; Ren, Z. T.; Cao, Y. H.; Li, Z.; Zhang, X. Hierarchical sheet-on-sheet heterojunction array of a β-$Ni(OH)_2$/$Fe(OH)_3$ self-supporting anode for effective overall alkaline water splitting. *Dalton Trans.* **2021**, *50*, 12547–12554.

[15] Yang, G. C.; Jiao, Y. Q.; Yan, H. J.; Xie, Y.; Wu, A. P.; Dong, X.; Guo, D. Z.; Tian, C. G.; Fu, H. G. Interfacial engineering of MoO_2–FeP heterojunction for highly efficient hydrogen evolution coupled with biomass electrooxidation. *Adv. Mater.* **2020**, *32*, 2000455.

[16] Ni, S.; Qu, H. N.; Xu, Z. H.; Zhu, X. Y.; Xing, H. F.; Wang, L.; Yu, J. M.; Liu, H. Z.; Chen, C. M.; Yang, L. R. Interfacial engineering of the $NiSe_2$/$FeSe_2$ p–p heterojunction for promoting oxygen evolution reaction and electrocatalytic urea oxidation. *Appl. Catal. B: Environ.* **2021**, *299*, 120638.

[17] Dai, T. Y.; Zhang, X.; Sun, M. Z.; Huang, B. L.; Zhang, N.; Da, P. F.; Yang, R.; He, Z. D.; Wang, W.; Xi, P. X. et al. Uncovering the promotion of CeO_2/$CoS_{1.97}$ heterostructure with specific spatial architectures on oxygen evolution reaction. *Adv. Mater.* **2021**, *33*, 2102593.

[18] Wang, L.; Zeng, Z. H.; Gao, W. P.; Maxson, T.; Raciti, D.; Giroux, M.; Pan, X. Q.; Wang, C.; Greeley, J. Tunable intrinsic strain in two-dimensional transition metal electrocatalysts. *Science* **2019**, *363*, 870–874.

[19] Li, H. G.; Di, S. L.; Niu, P.; Wang, S. L.; Wang, J.; Li, L. A durable half-metallic diatomic catalyst for efficient oxygen reduction. *Energy Environ. Sci.* **2022**, *15*, 1601–1610.

[20] Mu, X. Q.; Yuan, H. M.; Jing, H. Y.; Xia, F. J.; Wu, J. S.; Gu, X. Y.; Chen, C. Y.; Bao, J. C.; Liu, S. L.; Mu, S. C. Superior electrochemical water oxidation in vacancy defect-rich 1.5 nm ultrathin trimetal-organic framework nanosheets. *Appl. Catal. B: Environ.* **2021**, *296*, 120095.

[21] Callejas, J. F.; Read, C. G.; Roske, C. W.; Lewis, N. S.; Schaak, R. E. Synthesis, characterization, and properties of metal phosphide catalysts for the hydrogen-evolution reaction. *Chem. Mater.* **2016**, *28*, 6017–6044.

[22] Theerthagiri, J.; Murthy, A. P.; Lee, S. J.; Karuppasamy, K.; Arumugam, S. R.; Yu, Y.; Hanafiah, M. M.; Kim, H. S.; Mittal, V.; Choi, M. Y. Recent progress on synthetic strategies and applications of transition metal phosphides in energy storage and conversion. *Ceram. Int.* **2021**, *47*, 4404–4425.

[23] Zhang, Y.; Gao, L.; Hensen, E. J. M.; Hofmann, J. P. Evaluating the Stability of Co_2P electrocatalysts in the hydrogen evolution reaction for both acidic and alkaline electrolytes. *ACS Energy Lett.* **2018**, *3*, 1360–1365.

[24] Miao, J. J.; Teng, X.; Zhang, R.; Guo, P. F.; Chen, Y.; Zhou, X. H.; Wang, H. Q.; Sun, X. N.; Zhang, L. B. "Carbohydrate-universal" electrolyzer for energy-saving hydrogen production with Co_3FeP_x@NF as bifunctional electrocatalysts. *Appl. Catal. B: Environ.* **2020**, *263*, 118109.

[25] Li, J. M.; Kang, Y. M.; Lei, Z. Q.; Liu, P. Well-controlled 3D flower-like CoP_3/CeO_2/C heterostructures as bifunctional oxygen electrocatalysts for rechargeable Zn–air batteries. *Appl. Catal. B: Environ.* **2023**, *321*, 122029.

[26] Lu, X. F.; Gu, L. F.; Wang, J. W.; Wu, J. X.; Liao, P. Q.; Li, G. R. Bimetal–organic framework derived $CoFe_2O_4$/C porous hybrid nanorod arrays as high-performance electrocatalysts for oxygen evolution reaction. *Adv. Mater.* **2017**, *29*, 1604437.

[27] Huang, H. L.; Li, J. R.; Wang, K. K.; Han, T. T.; Tong, M. M.; Li, L. S.; Xie, Y. B.; Yang, Q. Y.; Liu, D. H.; Zhong, C. L. An *in situ* self-assembly template strategy for the preparation of hierarchical-pore metal–organic frameworks. *Nat. Commun.* **2015**, *6*, 8847.

[28] Zhang, C.; Huang, Y.; Yu, Y. F.; Zhang, J. F.; Zhuo, S. F.; Zhang, B. Sub-1.1 nm ultrathin porous CoP nanosheets with dominant reactive {200} facets: A high mass activity and efficient electrocatalyst for the hydrogen evolution reaction. *Chem. Sci.* **2017**, *8*, 2769–2775.

[29] Xiao, X. F.; He, C. T.; Zhao, S. L.; Li, J.; Lin, W. S.; Yuan, Z. K.;

Zhang, Q.; Wang, S. Y.; Dai, L. M.; Yu, D. S. A general approach to cobalt-based homobimetallic phosphide ultrathin nanosheets for highly efficient oxygen evolution in alkaline media. *Energy Environ. Sci.* **2017**, *10*, 893–899.

[30] Tian, J. Q.; Liu, Q.; Asiri, A. M.; Sun, X. P. Self-supported nanoporous cobalt phosphide nanowire arrays: An efficient 3D hydrogen-evolving cathode over the wide range of pH 0–14. *J. Am. Chem. Soc.* **2014**, *136*, 7587–7590.

[31] Wu, T. L.; Pi, M. Y.; Wang, X. D.; Zhang, D. K.; Chen, S. J. Three-dimensional metal–organic framework derived porous CoP_3 concave polyhedrons as superior bifunctional electrocatalysts for the evolution of hydrogen and oxygen. *Phys. Chem. Chem. Phys.* **2017**, *19*, 2104–2110.

[32] Li, Y. J.; Zhang, H. C.; Jiang, M.; Zhang, Q.; He, P. L.; Sun, X. M. 3D self-supported Fe-doped Ni_2P nanosheet arrays as bifunctional catalysts for overall water splitting. *Adv. Funct. Mater.* **2017**, *27*, 1702513.

[33] Li, Y. B.; Zhao, C. Enhancing water oxidation catalysis on a synergistic phosphorylated NiFe hydroxide by adjusting catalyst wettability. *ACS Catal.* **2017**, *7*, 2535–2541.

[34] Zhao, S. H.; Wang, T. Q.; Ji, Z. J.; Song, Y. J.; Li, Y.; Liu, J.; Hu, W. P. Spatial decoupling of dehydrogenation and CO oxidation by Ni–Co–Ti hierarchical trimetallic catalyst for electrocatalytic oxidation of methanol. *Appl. Catal. B: Environ.* **2023**, *320*, 122024.

[35] Zhao, B.; Liu, J. W.; Yin, Y. R.; Wu, D.; Luo, J. L.; Fu, X. Z. Carbon nanofibers@NiSe core/sheath nanostructures as efficient electrocatalysts for integrating highly selective methanol conversion and less-energy intensive hydrogen production. *J. Mater. Chem. A* **2019**, *7*, 25878–25886.

[36] Zhang, X. F.; Li, X. C.; Li, R. C.; Lu, Y.; Song, S. Q.; Wang, Y. Highly active core–shell carbon/$NiCo_2O_4$ double microtubes for efficient oxygen evolution reaction: Ultralow overpotential and superior cycling stability. *Small* **2019**, *15*, 1903297.

[37] Xin, Y.; Sun, L. P.; Huo, L. H.; Zhao, H. Co–Ni–P nanoneedle array heterostructures with built-in potential for selective methanol oxidation coupled with H_2 evolution. *ACS Appl. Nano Mater.* **2023**, *6*, 10312–10321.

[38] Xiang, K.; Wu, D.; Deng, X. H.; Li, M.; Chen, S. Y.; Hao, P. P.; Guo, X. F.; Luo, J. L.; Fu, X. Z. Boosting H_2 generation coupled with selective oxidation of methanol into value-added chemical over cobalt hydroxide@hydroxysulfide nanosheets electrocatalysts. *Adv. Funct. Mater.* **2020**, *30*, 1909610.

[39] Li, J. S.; Luo, Z. S.; He, F.; Zuo, Y.; Zhang, C. Q.; Liu, J. F.; Yu, X. T.; Du, R. F.; Zhang, T.; Infante-Carrió, M. F. et al. Colloidal Ni–Co–Sn nanoparticles as efficient electrocatalysts for the methanol oxidation reaction. *J. Mater. Chem. A* **2018**, *6*, 22915–22924.

[40] Siahroudi, M. G.; Daryakenari, A. A.; Molamahaleh, Y. B.; Cao, Q.; Daryakenari, M. A.; Delaunay, J. J.; Siavoshi, H.; Molaei, F. Ethylene glycol assisted solvo-hydrothermal synthesis of NGr–Co_3O_4 nanostructures for ethanol electrooxidation. *Int. J. Hydrogen Energy* **2020**, *45*, 30357–30366.

[41] Wang, W. B.; Zhu, Y. B.; Wen, Q. L.; Wang, Y. T.; Xia, J.; Li, C. C.; Chen, M. W.; Liu, Y. W.; Li, H. Q.; Wu, H. A. et al. Modulation of molecular spatial distribution and chemisorption with perforated nanosheets for ethanol electro-oxidation. *Adv. Mater.* **2019**, *31*, 1900528.

[42] Mushiana, T.; Khan, M.; Abdullah, M. I.; Zhang, N.; Ma, M. M. Facile sol–gel preparation of high-entropy multielemental electrocatalysts for efficient oxidation of methanol and urea. *Nano Res.* **2022**, *15*, 5014–5023.

[43] Hao, S. J.; Cong, M. Y.; Xu, H. W.; Ding, X.; Gao, Y. Bismuth-based electrocatalysts for identical value-added formic acid through coupling CO_2 reduction and methanol oxidation. *Small* **2024**, *20*, 2307741.

[44] Jiang, S.; Xiao, T. Y.; Xu, C.; Wang, S. W.; Peng, H. Q.; Zhang, W. J.; Liu, B.; Song, Y. F. Passivating oxygen evolution activity of NiFe-LDH through heterostructure engineering to realize high-efficiency electrocatalytic formate and hydrogen Co-production. *Small* **2023**, *19*, 2208027.

[45] Huang, Y. K.; Li, T.; Feng, H.; Lv, L. T.; Tang, T. X.; Lin, Z.; Ye, K. H.; Wang, Y. Q. High-valence co stabilized by *in-situ* growth of ZIF-67 on NiCo-LDH for enhanced performance in oxygen evolution reaction. *Small* **2025**, *21*, 2407443.

[46] Ren, X.; Li, M. G.; Qiu, L. Y.; Guo, X.; Tian, F. Y.; Han, G. H.; Yang, W. W.; Yu, Y. S. Cationic vacancies and interface engineering on crystalline-amorphous gamma-phase Ni–Co oxyhydroxides achieve ultrahigh mass/areal/volumetric energy density flexible all-solid-state asymmetric supercapacitor. *J. Mater. Chem. A* **2023**, *11*, 5754–5765.

[47] Jiang, N.; Yu, J. T.; Wu, Z. H.; Zhao, J. H.; Zeng, Y. Y.; Li, H. X.; Meng, M.; He, Y. T.; Jiao, P. X.; Pan, H. C. et al. Surface gradient desodiation chemistry in layered oxide cathode materials. *Angew. Chem., Int. Ed.* **2024**, *63*, e202410080.

[48] Zhong, J. Y.; Chen, Q. M.; Guo, C. X.; Peng, W. C.; Li, Y.; Zhang, F. B.; Fan, X. B. Al^{3+} leaching induced Co^{4+} on CoFeAl layered double hydroxide for enhanced oxygen evolution reaction. *Int. J. Hydrogen Energy* **2023**, *48*, 23530–23539.

[49] Chen, Z.; Kronawitter, C. X.; Yeh, Y. W.; Yang, X. F.; Zhao, P.; Yao, N.; Koel, B. E. Activity of pure and transition metal-modified CoOOH for the oxygen evolution reaction in an alkaline medium. *J. Mater. Chem. A* **2017**, *5*, 842–850.

[50] Huang, Y. C.; Wu, Y. J.; Lu, Y. R.; Chen, J. L.; Lin, H. J.; Chen, C. T.; Chen, C. L.; Jing, C.; Zhou, J.; Zhang, L. J. et al. Direct identification of O–O bond formation through three-step oxidation during water splitting by *operando* soft X-ray absorption spectroscopy. *Adv. Sci.* **2024**, *11*, 2470244.

[51] Lee, W. H.; Han, M. H.; Ko, Y. J.; Min, B. K.; Chae, K. H.; Oh, H. S. Electrode reconstruction strategy for oxygen evolution reaction: Maintaining Fe–CoOOH phase with intermediate-spin state during electrolysis. *Nat. Commun.* **2022**, *13*, 605.

[52] Rajan, A. P. S.; Senthil, R. A.; Moon, C. J.; Kumar, A.; Min, A.; Ubaidullah, M.; Choi, M. Y. Insights into dual-functional catalytic activity of laser-driven CoGaIr-LDH nanosheets in water electrolysis for green hydrogen production via *in-situ* Raman and theoretical analyses. *Chem. Eng. J.* **2024**, *502*, 157848.

[53] Qi, Y. B.; Zhu, Y. H.; Jiang, H. L.; Li, C. Z. Promoting electrocatalytic oxidation of methanol to formate through interfacial interaction in NiMo oxide-CoMo oxide mixture-derived catalysts. *Chin. J. Catal.* **2024**, *56*, 139–149.

[54] Han, J. R.; Wang, H. B.; Wang, Y. T.; Zhang, H.; Li, J.; Xia, Y. J.; Zhou, J. S.; Wang, Z. Y.; Luo, M. C.; Wang, Y. H. et al. Lattice oxygen activation through deep oxidation of Co_4N by Jahn–Teller-active dopants for improved electrocatalytic oxygen evolution. *Angew. Chem., Int. Ed.* **2024**, *63*, e202405839.

[55] Wu, T. Z.; Sun, S. N.; Song, J. J.; Xi, S. B.; Du, Y. H.; Chen, B.; Sasangka, W. A.; Liao, H. B.; Gan, C. L.; Scherer, G. G. et al. Iron-facilitated dynamic active-site generation on spinel $CoAl_2O_4$ with self-termination of surface reconstruction for water oxidation. *Nat. Catal.* **2019**, *2*, 763–772.

[56] Zhao, X.; Li, Y. Y.; Cui, Y.; Saqib, M.; Zhang, X. Y.; Hao, R.; Zheng, Z. P. Spatiotemporally and chemically resolved imaging of electrocatalytic oxygen evolution on single nanoplates of cobalt-layered hydroxide. *J. Am. Chem. Soc.* **2023**, *145*, 20897–20906.

[57] Wu, Q. B.; Liang, J. W.; Xiao, M. J.; Long, C.; Li, L.; Zeng, Z. H.; Mavrič, A.; Zheng, X.; Zhu, J.; Liang, H. W. et al. Non-covalent ligand-oxide interaction promotes oxygen evolution. *Nat. Commun.* **2023**, *14*, 997.

[58] Yang, H.; Li, F. S.; Zhan, S. Q.; Liu, Y. W.; Li, W. L.; Meng, Q. J.; Kravchenko, A.; Liu, T. Q.; Yang, Y.; Fang, Y. et al. Intramolecular hydroxyl nucleophilic attack pathway by a polymeric water oxidation catalyst with single cobalt sites. *Nat. Catal.* **2022**, *5*, 414–429.

[59] Li, D. Y.; Xiang, R.; Yu, F.; Zeng, J. S.; Zhang, Y.; Zhou, W. C.;

Liao, L. L.; Zhang, Y.; Tang, D. S.; Zhou, H. Q. *In situ* regulating cobalt/iron oxide–oxyhydroxide exchange by dynamic iron incorporation for robust oxygen evolution at large current density. *Adv. Mater.* **2024**, *36*, 2305685.

[60] Li, D. R.; Wan, W. J.; Wang, Z. W.; Wu, H. Y.; Wu, S. X.; Jiang, T.; Cai, G. X.; Jiang, C. Z.; Ren, F. Self-derivation and surface reconstruction of Fe-doped Ni_3S_2 electrode realizing high-efficient and stable overall water and urea electrolysis. *Adv. Energy Mater.* **2022**, *12*, 2201913.

[61] Ye, S. H.; Wang, J. P.; Hu, J.; Chen, Z. D.; Zheng, L. R.; Fu, Y. H.; Lei, Y. Q.; Ren, X. Z.; He, C. X.; Zhang, Q. L. et al. Electrochemical construction of low-crystalline CoOOH nanosheets with short-range ordered grains to improve oxygen evolution activity. *ACS Catal.* **2021**, *11*, 6104–6112.

[62] Meng, F. X.; Dai, C. C.; Liu, Z.; Luo, S. Z.; Ge, J. J.; Duan, Y.; Chen, G.; Wei, C.; Chen, R. R.; Wang, J. R. et al. Methanol electro-oxidation to formate on iron-substituted lanthanum cobaltite perovskite oxides. *Escience* **2022**, *2*, 87–94.

[63] Zhu, B. T.; Dong, B.; Wang, F.; Yang, Q. F.; He, Y. P.; Zhang, C. J.; Jin, P.; Feng, L. Unraveling a bifunctional mechanism for methanol-to-formate electro-oxidation on nickel-based hydroxides. *Nat. Commun.* **2023**, *14*, 1686.

[64] Fu, S. Q.; Ma, Y. R.; Yang, X. C.; Yao, X.; Jiao, Z.; Cheng, L. L.; Zhao, P. D. Defect and interface engineering of hexagonal $Fe_2O_3/ZnCo_2O_4$ n–n heterojunction for efficient oxygen evolution reaction. *Appl. Catal. B: Environ.* **2023**, *333*, 122813.

[65] Lu, Y. X.; Liu, T. Y.; Dong, C. L.; Yang, C. M.; Zhou, L.; Huang, Y. C.; Li, Y. F.; Zhou, B.; Zou, Y. Q.; Wang, S. Y. Tailoring competitive adsorption sites by oxygen-vacancy on cobalt oxides to enhance the electrooxidation of biomass. *Adv. Mater.* **2022**, *34*, 2107185.

[66] Lu, Y. X.; Liu, T. Y.; Huang, Y. C.; Zhou, L.; Li, Y. Y.; Chen, W.; Yang, L.; Zhou, B.; Wu, Y. D.; Kong, Z. J. et al. Integrated catalytic sites for highly efficient electrochemical oxidation of the aldehyde and hydroxyl groups in 5-hydroxymethylfurfural. *ACS Catal.* **2022**, *12*, 4242–4251.